Dopamine modulates the size of striatal projection neuron ensembles

Marta Maltese[1,2,*], Jeffrey R. March[1,2,*], Alexander G. Bashaw[1,2], Nicolas X. Tritsch[1,2,#]

[1] Neuroscience Institute, New York University School of Medicine, New York, NY 10016, U.S.A.
[2] Fresco Institute for Parkinson's and Movement Disorders, New York University Langone Health, New York, NY 10016, U.S.A.

[*] equal contribution
[#] correspondence and requests for materials should be addressed to N.X.T. (email: nicolas.tritsch@nyulangone.org)

SUMMARY

Dopamine (DA) is a critical modulator of brain circuits that control voluntary movements, but our understanding of its influence on the activity of target neurons *in vivo* remains limited. Here, we use two-photon Ca^{2+} imaging to simultaneously monitor the activity of direct and indirect-pathway spiny projection neurons (SPNs) in the striatum of behaving mice during acute and prolonged manipulations of DA signaling. We find that, contrary to prevailing models, DA does not modulate activity rates in either pathway strongly or differentially. Instead, DA exerts a prominent influence on the overall number of direct and indirect pathway SPNs recruited during behavior. Chronic loss of midbrain DA neurons in a model of Parkinson's disease selectively impacts direct pathway ensembles and profoundly alters how they respond to DA elevation. Our results indicate that DA regulates striatal output by dynamically reconfiguring its sparse ensemble code and provide novel insights into the pathophysiology of Parkinson's disease.

INTRODUCTION

The neuromodulator dopamine (DA) is an essential component of basal ganglia circuits that control goal-directed behaviors. Considerable evidence in humans, primates and rodents implicates DA in the selection and execution of vigorous movement and in supporting motor learning via its actions in striatum, the largest input nucleus of the basal ganglia (Graybiel 2005; Turner & Desmurget 2010; Dudman & Krakauer 2016; Klaus et al., 2019). In humans for instance,

loss of striatum-projecting midbrain DA neurons in Parkinson's disease is associated with bradykinesia, while drugs that elevate DA act as stimulants and are behaviorally reinforcing.

Striatal output is mediated by two populations of inhibitory spiny projection neurons (SPNs) belonging to the direct and indirect pathways (dSPNs and iSPNs). Although long believed to exert opposite effects on movement, dSPNs and iSPNs are now known to be concurrently active and to work in concert to produce coherent sequences of voluntary movements (Cui et al., 2013; Barbera et al., 2016; Klaus et al., 2017; Markowitz et al., 2018; Meng et al., 2018; Parker et al., 2018; Sheng et al., 2019). Both receive excitatory inputs from overlapping cortical and thalamic areas and modulatory afferents from midbrain DA neurons (Kress et al., 2013; Wall et al., 2013; Guo et al., 2015). Because dSPNs express $G\alpha_s$-coupled D1-type DA receptors and iSPNs $G\alpha_i$-coupled D2-type DA receptors, DA is thought to modulate both pathways in opposite ways and to promote imbalances that impact how the basal ganglia orchestrate and modify behavior (Gerfen & Surmeier 2011; Klaus et al., 2019). However, the cellular and circuit mechanisms of DA action *in vivo* remain poorly understood.

Electrophysiological studies *in vitro* have identified several ion channels and synaptic properties in SPNs susceptible to differential modulation by DA (Tritsch & Sabatini 2012; Zhai et al., 2019). A widely-held view is that DA increases the firing rate of dSPNs and depresses that of iSPNs (Nelson & Kreitzer 2014). Although supported by some chronic DA depletion studies modeling Parkinson's disease (Mallet et al., 2006; Parker et al., 2018; Ryan et al., 2018), others report no or even opposite changes in discharge rate under similar conditions (Liang et al., 2008; Ellens & Leventhal 2013; Willard et al., 2019). Additional aspects of striatal physiology susceptible to acute pathway-specific DA modulation, like bursting and synaptic efficacy have been comparatively less explored *in vivo*.

Recent imaging studies show that distinct motor actions are represented in striatum by separate groups – or ensembles – of SPNs, and that individual renditions of a given action recruit only a subset of SPNs from the larger action-specific ensemble (Barbera et al., 2016; Klaus et al., 2017; Markowitz et al., 2018). It is presently not clear how plastic these neural representations are, and if DA plays a role in sculpting them. Here, we test this possibility using two-photon Ca^{2+} imaging to monitor dSPN and iSPN ensembles simultaneously in the striatum of behaving mice. We report that acute DA manipulations strongly modify the overall size of movement-related dSPN and iSPN ensembles, while exerting comparatively little influence on the rate of Ca^{2+} events. In addition, we show that chronic loss of midbrain DA neurons in a model of Parkinson's disease is associated with a specific decrease in the number of active dSPNs and with significant changes in how dSPN ensembles respond to DA replacement.

RESULTS

Baseline activity in dSPNs and iSPNs is concurrent and balanced

To resolve the activity of individual striatal neurons *in vivo*, we performed two-photon microscopy through a chronically implanted window (Howe & Dombeck 2016; Bloem et al., 2017) in head-fixed mice (N = 18) on a freely rotating circular treadmill (**Fig. 1a**). We expressed the Ca^{2+} indicator GCaMP6f (Chen et al., 2013) virally in the dorsolateral striatum under control of the synapsin promoter to label all neurons. Experiments were conducted using *Drd1a*^{tdTomato} transgenic mice, in which dSPNs are selectively labeled red (Ade et al., 2011). This approach allows differentiation of Ca^{2+} signals arising in dSPNs from those in tdTomato-negative neurons, which are overwhelmingly iSPNs, and which together with dSPNs account for over 90% of all striatal neurons (Gerfen & Surmeier 2011). We obtained large fields of view (FOV; 500 x 500 μm, n = 1–3 per mouse) with clearly identifiable dSPNs interspersed among neurons containing GCaMP6f only (**Fig. 1b** and **Supplementary Video**).

Self-paced forward locomotion was associated with prominent increases in fluorescence in groups of neurons both positive and negative for tdTomato (**Fig. 1c**). Population Ca^{2+} signals in tdTomato-positive dSPNs resembled data obtained using photometry in mice expressing GCaMP6f selectively in dSPNs (**Supplementary Fig. 1a**). Amongst tdTomato-negative neurons, the vast majority resembled dSPNs in morphology and, when active, showed Ca^{2+} transients comparable to those observed in dSPNs (**Fig. 1e,f**) and activity consistent with signals obtained specifically from iSPNs (**Supplementary Fig. 1b–d**). These cells were consequently classified as iSPNs. A small fraction of tdTomato-negative neurons consistently exhibited distinct Ca^{2+} dynamics, suggesting that they represent striatal interneurons (Gritton et al., 2019; Howe et al., 2019). Indeed, the proportions of imaged neurons assigned to dSPNs, iSPNs and interneurons agree with anatomical estimates (**Fig. 1d**). This imaging approach therefore offers the ability to simultaneously monitor and compare the activity of hundreds of striatal neurons (mean ± SEM): 327 ± 13 per FOV, range: 131–442) belonging to both direct and indirect pathways with high spatial resolution during a simple behavior.

The fraction of all imaged dSPNs and iSPNs displaying Ca^{2+} transients in each FOV across all forward locomotor bouts were comparable across imaging sessions on separate days (**Fig. 1g,h**), with a slightly greater proportion of active iSPNs as compared to dSPNs (active iSPNs: 20.5 ± 2.2 % of all imaged iSPNs; active dSPNs: 18.0 ± 2.2 % of all imaged dSPNs; $p = 0.022$, Wilcoxon signed-rank; **Fig. 1i**). Forward locomotion was associated with the activation of a sparse subset of SPNs from the larger ensembles defined across several locomotor bouts. The number of SPNs contributing to each subset grew larger as treadmill speed increased without notable temporal offset between pathways (**Fig. 1j,k**). The end of movement was associated with a progressive decline in the fraction of active SPNs (**Fig. 1k**). The frequency of Ca^{2+} transients in individual SPNs

was also comparable across pathways and similarly reflected treadmill velocity (**Fig. 1l–n**). Thus, consistent with previous reports (Barbera et al., 2016; Klaus et al., 2017; Markowitz et al., 2018), self-paced forward locomotion is associated with sparse activation of subsets of SPNs that over time define larger, action-related ensembles, with few notable differences distinguishing dSPNs from iSPNs at either low (< 0.2 cm/s; i.e. immobile) or high (> 0.4 cm/s) treadmill speeds.

DA neuron lesions impact population-level Ca^{2+} event rates

To estimate the influence of DA on striatal activity, we first injected the neurotoxin 6-hydroxydopamine (6-OHDA) into the substantia nigra pars compacta (SNc) ipsilateral to the striatal hemisphere under investigation in a subset of mice (N = 12). This manipulation causes DA neurons to degenerate within hours, resulting in near complete and irreversible loss of tyrosine hydroxylase (TH)-positive cell bodies in SNc and commensurate reductions in DA transporter (DAT) fluorescence in dorsal striatum (**Fig. 2a,b** and **Supplementary Fig. 2a,b**). Consistent with DA's established role in producing vigorous movement (Panigrahi et al., 2015), unilateral SNc lesions mildly reduced the mean velocity of self-paced locomotor bouts compared to sham-treated mice (N = 6; Two-way ANOVA lesion x time: $F_{2,30} = 5.56$, $p = 0.009$) as early as 24 hours and for up to a month after treatment (**Supplementary Fig. 2c**), but not their duration ($F_{2,30} = 0.99$, $p = 0.38$; **Supplementary Fig. 2d**) or frequency ($F_{2,30} = 0.15$, $p = 0.86$; **Supplementary Fig. 2e**). Lesioned mice also showed a strong and persistent ipsiversive turning bias in a closed-arm plus-maze ($F_{2,27} = 6.0$, $p = 0.007$; **Fig. 2c**), further providing evidence of the immediate and long-lasting motor impairments that result from unilateral loss of SNc neurons.

A recent study using one-photon microendoscopy revealed that DA depletion results in large and opposite changes in the frequency of Ca^{2+} transients imaged from dSPNs and iSPNs in separate cohorts of freely behaving mice (Parker et al., 2018). We therefore attempted to replicate their findings under our experimental conditions by monitoring Ca^{2+} signals in dSPNs and iSPNs concurrently within the same FOV. We first confirmed that DA depletion (n = 21 FOVs in 12 mice) did not compromise our ability to detect Ca^{2+} transients, as their amplitude in dSPNs and iSPNs did not significantly vary over imaging sessions compared to sham-treated mice (n = 9 FOVs in 6 mice; Two-way ANOVA lesion x time: dSPN: $F_{2,45} = 1.31$, $p = 0.3$; iSPN: $F_{2,45} = 1.50$, $p = 0.2$; **Supplementary Fig. 3a–c**), excluding shifts in signal-to-noise as primary contributors to 6-OHDA-mediated phenotypes. In agreement with Parker and colleagues (2018), we observed a significant effect of 6-OHDA on the overall rate of Ca^{2+} events imaged across the entire FOV (i.e. population-level Ca^{2+} event rate) in both dSPNs (Two-way ANOVA lesion x time: $F_{2,45} = 3.95$, $p = 0.026$) and iSPNs ($F_{2,45} = 14.84$, $p = 1.12 \times 10^{-5}$) compared to vehicle-treated mice. Striatal activity did not appreciably change in sham-treated mice, establishing a stable baseline from which to identify differences specifically related to the loss of DA neurons. By contrast, population-level rates in dSPNs decreased by half during locomotion immediately after 6-OHDA infusion, while

146 they more than doubled in iSPNs at all recorded velocities (**Fig. 2d–i**). Population-level Ca^{2+} event
147 rates in chronically lesioned mice remained depressed in dSPNs but returned to baseline in iSPNs
148 during movement (**Fig. 2d–i**), consistent with previous observations (Parker et al., 2018). These
149 results therefore indicate that DA depletion strongly biases striatum-wide activity towards the
150 indirect pathway both acutely and chronically in head-fixed and freely-moving mice. However,
151 they do not clearly establish how these population-level effects arise. We investigate this in the
152 following section.
153
154 **Lesioning DA neurons differentially alters dSPN and iSPN ensemble size**

155 The population-level Ca^{2+} event rate changes reported in **Fig. 2** may result from changes in
156 the frequency of Ca^{2+} transients experienced by individual SPNs, differences in the overall size of
157 SPN ensembles recruited by a given behavior, or both (**Fig. 3a**). To distinguish between these
158 possibilities, we took advantage of the high spatial resolution and signal-to-noise of two-photon
159 microscopy (Helmchen & Denk 2005). Given our reported effects on frequency (**Fig. 2**) and the
160 prevalence of rate-based models of basal ganglia function and DA modulation (reviewed in
161 Calabresi et al., 2014; Nelson & Kreitzer 2014), we first asked whether acute and chronic DA
162 depletion alters the frequency of Ca^{2+} transients in individual SPNs. Surprisingly, we failed to
163 detect a significant effect of 6-OHDA compared to sham in either dSPNs (Two-way ANOVA lesion
164 x time: $F_{2,45}$ = 1.05, p = 0.36; **Fig. 3b**) or iSPNs ($F_{2,45}$ = 1.64, p = 0.21; **Fig. 3c**) across recorded
165 treadmill velocities (**Fig. 3e**). Because the mean Ca^{2+} transient frequency per active iSPN trended
166 up immediately after 6-OHDA infusion and trended down in dSPNs in chronically lesioned mice,
167 DA depletion did result in a slight imbalance in activity rates towards the indirect pathway ($F_{2,45}$
168 = 7.98, p = 0.001; **Fig. 3d**). However, this effect alone cannot account for the strongly
169 dichotomous behavior of dSPNs and iSPNs reported above (**Fig. 2**) and before (Parker et al.,
170 2018).

171 We therefore considered the alternative possibility that lesioning DA neurons alters the size
172 of SPN ensembles associated with forward locomotion. Indeed, we observed a strong effect of 6-
173 OHDA on ensemble size compared to vehicle-injected mice in dSPNs (Two-way ANOVA lesion x
174 time: $F_{2,53}$ = 3.66, p = 0.03; **Fig. 3f**), iSPNs ($F_{2,53}$ = 11.92, p = 5.3 x 10^{-5}; **Fig. 3g**) and in pathway bias
175 ($F_{2,53}$ = 19.0, p = 6.1 x 10^{-7}; **Fig. 3h**). Specifically, the total number of dSPNs displaying Ca^{2+}
176 transients over the course of an imaging session was halved immediately after 6-OHDA infusion
177 and remained low thereafter (**Fig. 3f**). This is unlikely to result from diminished locomotor speed
178 because within the same FOV, the total number of active iSPNs and the subset of iSPNs recruited
179 per locomotor bout doubled in acutely lesioned mice (**Fig. 3g**) across recorded velocities (**Fig. 3i**)
180 and movement bouts (**Fig. 3j**). In addition, imaging sessions on motorized treadmills with
181 constant velocity and distance traveled yielded similar results (**Supplementary Fig. 3j–l**). Acute
182 loss of SNc neurons therefore alters the extent of dSPN and iSPN ensembles in opposite ways,

183 generating a strong imbalance in favor of the indirect pathway (**Fig. 3h**). Interestingly, the
184 expansion of iSPN ensembles was not sustained in time and returned to baseline in chronically
185 lesioned animals (**Fig. 3f–j**). Because compensatory changes were not observed in dSPNs, the
186 overall size of SPN ensembles recruited over the course of imaging sessions remained
187 significantly biased towards the indirect pathway in chronically lesioned mice (**Fig. 3h**).
188

189 **DA receptor signaling rapidly reconfigure SPN ensembles**

190 Neurotoxic lesions cannot reveal DA's dynamic modulatory actions and only implicate DA
191 indirectly, as SNc neurons release multiple transmitters (Trudeau et al., 2014) and 6-OHDA-
192 mediated cell death triggers inflammatory responses (Cicchetti et al., 2002). To more directly
193 assess DA's influence on striatal activity on the time scale of minutes, we compared SPN Ca^{2+}
194 signals before and after systemic administrations of a cocktail of DA receptor antagonists in DA-
195 intact mice. Under our experimental conditions, this manipulations did not affect mean velocity
196 or bout duration, but significantly curtailed the number of spontaneously-initiated locomotor
197 bouts compared to vehicle-treated animals (**Supplementary Fig. 4a–c**). We therefore limited our
198 analyses to imaging sessions on motorized treadmills to keep velocity and distance traveled
199 constant.

200 Consistent with our earlier findings, reducing DA signaling did not change the frequency of
201 Ca^{2+} transients in individual dSPNs recruited by forward locomotion ($p = 0.2$, Mann-Whitney;
202 vehicle: n = 10 FOVs in 5 mice; DA antagonist: n = 11 FOVs in 5 mice; **Fig. 4a**). The frequency of
203 Ca^{2+} transients in iSPNs increased ($p = 0.007$, Mann-Whitney; **Fig. 4b**), but not enough to bias
204 striatal activity towards the indirect pathway ($p = 0.22$, Mann-Whitney; **Fig. 4c**). In stark contrast,
205 blocking DA receptors significantly affected SPN ensemble size: it reduced the total number of
206 dSPNs recruited by forward locomotion by half ($p = 0.006$, Mann-Whitney; **Fig. 4d**) and expanded
207 iSPNs more than three-fold ($p = 5.7 \times 10^{-6}$, Mann-Whitney; **Fig. 4e**), leading to a strong imbalance
208 in favor of the indirect pathway ($p = 5.7 \times 10^{-6}$, Mann-Whitney; **Fig. 4f**). These data indicate that
209 loss of DA minimally impacts the frequency of Ca^{2+} transients displayed by SPNs, yet it evokes
210 substantial reconfiguration of the overall number of dSPNs and iSPNs associated with a given
211 behavior.

212 We next investigated whether elevating DA signaling would exert the opposite effect. To do
213 so, we imaged striatal activity upon pharmacological stimulation of D1 and D2 receptors (n = 11
214 FOVs in 7 mice) while mice locomoted on motorized treadmills to mitigate treatment effects on
215 spontaneous behavior (**Supplementary Fig. 4a–c**). Here too, we failed to detect changes in the
216 frequency of Ca^{2+} transients during locomotion in individual dSPNs ($p = 0.9$, Mann-Whitney; **Fig.**
217 **4a**) or between pathways ($p = 0.36$, Mann-Whitney; **Fig. 4c**), despite a small but statistically
218 significant decrease in Ca^{2+} transient frequency in iSPNs compared to vehicle ($p = 0.021$, Mann-
219 Whitney; **Fig. 4b**). By contrast, stimulating DA receptors markedly altered the size of SPN

220 ensembles associated with forward locomotion, yielding a strong imbalance in favor of the direct
221 pathway ($p = 2.0 \times 10^{-4}$, Mann-Whitney; **Fig. 4f**). The latter was mediated by a near complete
222 decline in the prevalence of active iSPNs ($p = 2.3 \times 10^{-5}$, Mann-Whitney; **Fig. 4e**) since, contrary
223 to DA's presumed excitatory influence on dSPNs, activation of DA receptors also diminished the
224 number of active dSPNs ($p = 0.015$, Mann-Whitney; **Fig. 4d**). Importantly, mild elevation of
225 endogenous DA using the presynaptic DA reuptake antagonist nomifensine similarly diminished
226 the number of active dSPNs without altering Ca^{2+} transient frequency (**Supplementary Fig. 4d,**
227 **e**). Together, these data indicate that DA does not strongly modulate the frequency of Ca^{2+}
228 transients in individual dSPNs and iSPNs that comprise action-specific ensembles. Instead, DA
229 controls the number of SPNs recruited with each motor action as well as the extent of the larger
230 SPN ensembles that are defined over multiple rendition of such action. While the overall number
231 of iSPNs recruited in this task is inversely related to extracellular DA, dSPNs follow an 'inverted-
232 U' shaped function, where too little or too much DA negatively impacts the size of their ensemble.
233

234 **Chronic DA depletion alters how SPN ensembles respond to DA**

235 Motor impairments in Parkinson's disease are typically managed by elevating striatal DA with
236 L-DOPA, the metabolic precursor for DA. We therefore wondered whether acutely restoring DA
237 with L-DOPA would affect SPN ensemble size, and if so how. To address this, we treated a subset
238 of the mice (N = 6) that had received unilateral vehicle or 6-OHDA infusions in SNc a month or
239 more earlier with a single dose of L-DOPA. As expected, this treatment had a significant effect on
240 the behavior of 6-OHDA vs. sham-lesioned mice (N = 5) in the plus-maze (Two-way ANOVA lesion
241 x levodopa: $F_{1,18} = 94.7$, $p = 1.4 \times 10^{-8}$), reversing the turning bias of lesioned mice within minutes
242 ($p = 6.2 \times 10^{-10}$, post-hoc Bonferroni; **Fig. 5a**). In the striatum of DA-depleted mice locomoting on
243 motorized treadmills (n = 12 FOVs), L-DOPA elevated the frequency of Ca^{2+} transients in individual
244 dSPNs and reversed the mild frequency imbalance caused by DA depletion (**Fig. 5c**), in agreement
245 with previous work (Parker et al., 2018). In addition and most notably, L-DOPA significantly
246 altered the size of SPN ensembles (**Fig. 5b**): it halved the overall number of iSPNs exhibiting Ca^{2+}
247 transients and expanded the number of active dSPNs 10-fold, reaching upwards of 70% of all
248 imaged dSPNs in some FOVs (**Fig. 5d**). This resulted in a reversal of ensemble size imbalance in
249 DA-depleted mice towards the direct pathway (**Fig. 5d**). These data therefore indicate that DA
250 favors the recruitment of dSPNs relative to iSPNs in both DA-intact and DA-depleted mice, but
251 that the underlying mechanisms profoundly differ (**Fig. 5e**).

DISCUSSION

In this study, we sought to reveal how acute and prolonged manipulations of DA signaling impact striatal output. To do so, we simultaneously monitored intracellular Ca^{2+} signals in dSPNs and iSPNs using two-photon microscopy to permit the identification of subtle imbalances between SPN populations long proposed to lie at the heart of basal ganglia function and dysfunction (Nelson & Kreitzer 2014; Klaus et al., 2019). We specifically examined changes in the frequency and amplitude of Ca^{2+} transients exhibited by individual neurons, in addition to changes in the overall size of SPN ensembles, all during a low-dimensional locomotor behavior to facilitate comparisons across imaging sessions.

In agreement with prior imaging studies (Cui et al., 2013; Barbera et al., 2016; Klaus et al., 2017; Markowitz et al., 2018; Meng et al., 2018; Parker et al., 2018), we found that the activity of dSPNs and iSPNs is balanced and concurrently elevated during movement under baseline conditions. Individual forward locomotion bouts recruited a subset of the overall ensemble of SPNs associated with that behavior in proportion to treadmill velocity. Individual dSPNs and iSPNs were not systematically activated across different locomotor bouts, at particular phases within movement bouts or at specific treadmill velocities, arguing against a specific role for individual SPNs in the initiation, maintenance or cessation of self-paced locomotion (Sales-Carbonell et al., 2018). Instead, these observations are consistent with dorsolateral striatum relying on a sparse ensemble code to guide behavior (Barbera et al., 2016; Klaus et al., 2017; Markowitz et al., 2018). The latter may result from a combination of anatomical and functional features proper to striatal neurons and circuits (Wilson & Kawaguchi 1996; Kincaid et al., 1998; Tepper et al., 2008; Ponzi & Wickens 2013; Reig & Silberberg 2014), and from the dynamic and heterogeneous activity of their excitatory (Churchland & Shenoy 2007; Robbe 2018; Sauerbrei et al., 2018) and modulatory inputs (Howe & Dombeck 2016; da Silva et al., 2018).

Changing DA levels or DA receptor signaling appreciably altered striatal activity, but not in a manner predicted by rate-based models of dopaminergic action (Calabresi et al., 2014; Nelson & Kreitzer 2014), as any effect on Ca^{2+} transient frequency in individual SPNs was generally mild and comparable across pathways. Indeed, acute DA manipulations did not modify the frequency of Ca^{2+} transients in dSPNs or produce large rate imbalances between pathways despite slight but significant frequency changes in iSPNs. We also failed to detect consistent effects on Ca^{2+} transient amplitude. Our results stand in contrast to a recent imaging study reporting changes in the rate of Ca^{2+} events in SPNs upon acute and chronic DA manipulations in freely behaving mice (Parker et al., 2018). This inconsistency may result from technical differences: we carried out experiments on motorized treadmills to promote movement at defined speeds and mitigate behavioral confounds. In addition, our imaging approach clearly distinguishes changes in the frequency and amplitude of Ca^{2+} transients per active neuron from changes in the overall number

289 of active cells (**Fig. 3a**), which can more easily be conflated with one-photon endoscopic
290 techniques (Helmchen & Denk 2005; Ziv & Ghosh 2015; Zhou et al., 2018). Accordingly, we ascribe
291 most of the changes in Ca^{2+} event rate observed at the population level (**Fig. 2**) to modifications
292 in the overall number of SPNs recruited during behavior.

293 Still, our observations may be surprising in light of previous reports of DA-dependent changes
294 in firing rates measured electrophysiologically. Because many such studies do not distinguish
295 dSPNs from iSPNs, it is conceivable that both populations comprise neurons that elevate and
296 depress their firing rates, resulting in little to no net change at the population level. Indeed, Ryan
297 and colleagues (2018) did not detect mean firing rate differences in iSPNs during movement in
298 chronically lesioned mice, in line with our findings (**Fig. 3c**). Alternatively, because
299 somatodendritic Ca^{2+} elevations in SPNs are tightly correlated with bursts of action potentials
300 (Kerr & Plenz 2002) and modulated by local interneurons independently of mean firing rate
301 (Owen et al., 2018), GCaMP6f fluorescence may not be sensitive to moderate changes in firing
302 rate and is more likely to reflect bursting activity patterns. As such, Ca^{2+} signals constitute a
303 measure of neural activity in their own right, highlighting bursting events likely to impact synaptic
304 plasticity in SPNs (Carter & Sabatini 2004; Jedrzejewska-Szmek et al., 2017) and discharge
305 patterns in downstream nuclei (Ellens & Leventhal 2013; Willard et al., 2019). Importantly, our
306 data indicate that the factors that control the rate of Ca^{2+} transients are neither strongly nor
307 differentially modulated by DA, pointing to a common synaptic drive to dSPNs and iSPNs.

308 By far the largest and most consistent effects of DA manipulations were changes in the overall
309 size of SPN ensembles associated with forward locomotion (**Fig. 5e**). Specifically, reducing DA
310 signaling rapidly depressed the total number of dSPNs exhibiting Ca^{2+} transients and
311 simultaneously doubled that of iSPNs, causing a strong imbalance in favor of the indirect
312 pathway. This supports the notion that DA normally acts to promote the recruitment of dSPNs
313 while limiting that of iSPNs. Interestingly, elevating DA signaling beyond physiological levels using
314 DA receptor agonists or a DA transporter inhibitor did not promote the opposite. Instead, both
315 dSPN and iSPN ensembles shrank. This observation challenges the implicit notion that high DA
316 levels invariably promote activation of the direct pathway. Thus, iSPN ensemble size is inversely
317 related to extracellular DA, whereas dSPN ensembles follows an "inverted-U" shaped response.
318 Interestingly, a similar relationship has been extensively described in prefrontal cortex with DA
319 acting on D1 receptors to regulate cognitive functions such as working memory (Vijayraghavan
320 et al., 2007), pointing to a common mechanism of dopaminergic modulation across brain areas.

321 It is increasingly recognized that motor impairments in Parkinson's disease reflect aberrant
322 activity patterns within the basal ganglia that arise not only from striatal DA loss, but also from
323 subsequent homeostatic circuit adaptations (Zhai et al., 2019). The latter are also believed to
324 underlie the dyskinetic side effects that result from chronic DA replacement therapy (Cenci 2014;
325 Picconi et al., 2018). Consistent with this, we observed stark differences in striatal activity

326 between acute and persistent loss of DA. In iSPNs, ensemble size returned to pre-lesion values in
327 chronically lesioned mice. These and other recent data (Ketzef et al., 2017; Parker et al., 2018;
328 Ryan et al., 2018; Willard et al., 2019) do not support the long- and widely-held notion that
329 persistent DA depletion in Parkinson's disease results in uncontrolled disinhibition of the indirect
330 pathway. Instead, they reveal a remarkable capacity for homeostatic plasticity in iSPNs reflected
331 in diminished intrinsic excitability, dendritic atrophy, spine loss and elevated inhibition from
332 surrounding interneurons (Gittis & Kreitzer 2012; Zhai et al., 2019).

333 By contrast, dSPNs failed to show functional recovery from acute DA loss, as few dSPNs
334 displayed Ca^{2+} signals up to a month after 6-OHDA injection, despite an increase in intrinsic
335 excitability (Fieblinger et al., 2014; Ketzef et al., 2017). This echoes previous observations that
336 dSPNs are more difficult to sample electrophysiologically and to evoke activity from in chronically
337 lesioned animals (Mallet et al., 2006), possibly because the number and strength of excitatory
338 inputs onto these cells declines (Fieblinger et al., 2014; Parker et al., 2016; Ketzef et al., 2017)
339 and GABAergic transmission rises (Lemos et al., 2016). This diminished ability to recruit dSPNs
340 may underlie the bradykinesia that defines Parkinson's disease. Interestingly, homeostatic
341 adaptions in dSPNs appear to rely more heavily on DA receptor signaling than in iSPNs, as chronic
342 DA depletion drastically altered how dSPNs respond to DA receptor stimulation, leading to
343 excessive recruitment of dSPNs not normally associated with forward locomotion. The resulting
344 degradation of action-selective dSPN ensembles may help explain why long-term L-DOPA
345 treatment eventually induces uncontrolled involuntary movements (Cenci 2014; Picconi et al.,
346 2018).

347 Together, our data indicate that the size of SPN ensembles encoding motor actions is not
348 fixed, but is rather dynamically modulated by DA. Thus, in addition to its established role in
349 shaping plasticity at individual synapses (Shen et al., 2008), DA also regulates the number of
350 neurons eligible to participate in such plasticity. In doing so, DA may directly contribute to the
351 production of vigorous motor actions (Panigrahi et al., 2015; da Silva et al., 2018; Yttri & Dudman
352 2018) and the refinement of motor skills (Yin et al., 2009; Sheng et al., 2019). Interestingly, DA
353 does this without strongly or differentially modulating the frequency of Ca^{2+} transients in dSPNs
354 or iSPNs. Instead, DA may regulate the number of SPNs that 'tune in' to a common input driving
355 somatodendritic Ca^{2+} spikes, a key element governing plasticity across brain areas in health and
356 disease (Lerner & Kreitzer 2011; Zhuang et al., 2013; Bittner et al., 2017; Nanou & Catterall 2018).
357 Future investigations will determine the cellular mechanisms that underlie this ability, the time
358 course of such changes in response to synaptic release of DA, and the impact of varying ensemble
359 size on the production and learning of motor actions by the basal ganglia.

ACKNOWLEDGEMENTS

We thank Adam Carter, Un Kang, Michael Long, Adam Mar, Margaret Rice, Dick Tsien and members of the Tritsch laboratory for comments on the manuscript. We thank the GENIE Program and the Janelia Research Campus, specifically V. Jayaraman, R. Kerr, D. Kim, L. Looger, and K. Svoboda for making GCaMP6f available. M.M. is supported by a Marlene and Paolo Fresco Postdoctoral Fellowship. N.X.T. is an Alfred P. Sloan Research Fellow in Neuroscience, and is supported by grants from the Dana, Leon Levy and Whitehall Foundations, as well as from the National Institutes of Health (R00NS087098 and DP2NS105553).

AUTHOR CONTRIBUTIONS

N.X.T. conceived of the project. M.M., J.R.M. and N.X.T. designed and performed experiments, analyzed and interpreted the data, and wrote the manuscript. A.G.B. helped with behavioral training and analysis.

DECLARATION OF INTERESTS

The authors declare no competing interests.

METHODS

Animals. All procedures were performed in accordance with protocols approved by the NYU Langone Health Institutional Animal Care and Use Committee. Mice were housed in group before surgery and singly after surgery under a reverse 12-hour light-dark cycle (dark from 10 a.m. to 10 p.m.) with *ad libitum* access to food and water. *Drd1a*^{tdTomato} transgenic mice were purchased from The Jackson Laboratory (stock #: 016204) and bred with C57BL/6J wild type mice (stock #: 000664). Transgenic mice expressing Cre selectively in iSPNs (*Adora2a*^{Cre_KG139}) or dSPNs (*Drd1a*^{Cre_EY217}) were generously provided by Chip Gerfen (NIH) and maintained on a C57BL/6J background. Control experiments in **Supplementary Fig. 1** were performed using offspring of *Adora2a*^{Cre_KG139} mice bred to a tdTomato reporter (Ai14; The Jackson Laboratory, Stock #: 007908). Experiments were carried out using both male and female mice heterozygous for all transgenes at 8–24 weeks of age.

397 **Surgery.** Mice were administered Dexamethasone (4 mg/kg, intraperitoneal) 1–2 hours prior to
398 surgery. They were then anaesthetized with isoflurane, placed in a stereotaxic apparatus (Kopf
399 Instruments) on a heating blanket (Harvard Apparatus) and administered Ketoprofen (10 mg/kg,
400 subcutaneous). The scalp was shaved and cleaned with ethanol and iodine solutions before
401 exposing the skull. A custom titanium headpost was implanted over lambda using C&B metabond
402 (Parkell) to allow head fixation. To achieve widespread viral expression of GCaMP6f in striatum,
403 100 nl of AAV1-Syn-GCaMP6f-WPRE-SV40 (University of Pennsylvania Vector Core) was injected
404 1.7 mm below dura at a rate of 100 nl/min (KD Scientific) into the right dorsolateral striatum at
405 four locations (anterior/lateral from bregma, in mm): 0.7/1.7; 0.7/2.3; 1.3/1.7 and 1.3/2.3.
406 Injection pipettes were left in place for 5 min before removal. A 3 mm craniotomy was then
407 drilled (centered at 1.0 mm anterior and 2.0 mm lateral from bregma) and cortical tissue was
408 aspirated until the corpus callosum lying above the striatum was exposed, as described previously
409 (Howe & Dombeck 2016). A custom 9 gauge thin-walled stainless-steel cannula (Microgroup; 2.3
410 mm in height) sealed at one end with a 3 mm glass coverslip (Warner Instruments) using optical
411 glue (Norland #71) was placed above the striatum and cemented to the skull using C&B
412 metabond. Mice were allowed to recover in their cage for 2 weeks before head-fixation
413 habituation, treadmill training and imaging.
414
415 **6-OHDA lesions.** For experiments characterizing the effects of SNc neuron loss on striatal activity,
416 a second stereotaxic surgery was performed under isoflurane anesthesia after baseline imaging
417 sessions. Desipramine (25 mg/kg) and pargyline (5 mg/kg) were administered intraperitoneally
418 prior to surgery to increase the selectivity and efficacy of 6-OHDA lesions (Thiele et al., 2012). A
419 small craniotomy was performed above the SNc ipsilateral to the imaged striatum (-3.1 mm
420 posterior from bregma, 1.3 mm lateral) and 3 μg of 6-OHDA (total volume: 200 nl) was injected
421 in SNc (4.2 mm below dura) at a rate ~100 nl/min. Sham-lesioned mice were treated identically
422 except that 6-OHDA was omitted from the injected solution (0.2% ascorbic acid in 0.9% sterile
423 NaCl solution). To evaluate motor impairments, mice were placed in a plus maze consisting of 4
424 identical arms (45 cm × 7 cm × 15 cm) at 90° to each other and monitored from above with a near
425 infrared camera (Basler; acA2000-165um) for 10 min. The number of ipsiversive, contraversive
426 and straight choices upon reaching the center of the maze were automatically quantified in
427 MATLAB (Mathworks) and verified visually. Data were expressed as a turning bias index, defined
428 as the difference between ipsiversive and contraversive turns, divided by the total number of
429 turns.
430
431 **Immunohistochemistry.** Mice were deeply anesthetized with isoflurane and perfused
432 transcardially with 4 % paraformaldehyde in 0.1 M sodium phosphate buffer. Brains were post-
433 fixed for 1–3 days, sectioned coronally (50–100 μm in thickness) using a vibratome (Leica;
434 VT1000S) and processed for immunofluorescence staining for tyrosine hydroxylase (Millipore;

435 AB152, 1:1000) and dopamine transporter (Millipore; MAB369, 1:1000) using standard methods.
436 Brain sections were mounted on superfrost slides and coverslipped with ProLong antifade
437 reagent with DAPI (Molecular Probes). Endogenous tdTomato and GCaMP6 fluorescence were
438 not immuno-enhanced. Whole sections were imaged with an Olympus VS120 slide scanning
439 microscope and high resolution images of regions of interest were subsequently acquired with a
440 Zeiss LSM 800 confocal microscope. TH and DAT immunofluorescence were quantified in ImageJ
441 (NIH) by measuring mean pixel intensity in similarly-sized regions of interest in VTA, SNc, dorsal
442 striatum and ventral striatum in both intact and lesioned hemispheres. After subtracting
443 background signal from adjacent unstained brain regions, fluorescence intensity values in the
444 lesioned hemisphere were expressed as a percentage of values measured on the intact side.
445 Three measurements were obtained from each region of interest along the anterior-posterior
446 axis and averaged together for each mouse.
447
448 **Reagents.** Drugs (all from Tocris, unless specified otherwise) were reconstituted and stored
449 according to the manufacturers' recommendations. 6-hydroxydopamine (6-OHDA; Sigma-
450 Aldrich) was dissolved freshly into sterile 0.9% NaCl and 0.2% ascorbic acid immediately prior to
451 administration to minimize oxidation. Working concentration aliquots of desipramine (25
452 mg/kg), pargyline (Sigma-Aldrich; 5 mg/kg), S(-)raclopride (Sigma-Aldrich; 1 mg/kg), SCH23390
453 (Fisher Scientific; 0.2 mg/kg), nomifensine (10 mg/kg), (-)quinpirole (3 mg/kg), SKF81297 (3
454 mg/kg) and L-DOPA (10 mg/kg) were prepared daily in sterile physiological saline and
455 administered intraperitoneally at minimum 20 min prior to experimentation. L-DOPA was co-
456 administered along with the peripheral DOPA decarboxylase inhibitor benserazide hydrochloride
457 (Sigma-Aldrich, 12 mg/kg).
458
459 **Two-Photon Imaging.** Imaging was performed through a 20X long working-distance air objective
460 (Edmund Optics; #58373) on a galvo-resonant scanning microscope (Thorlabs; Bergamo-II)
461 equipped with GaAsP photomultiplier tubes and under the control of ScanImage 5 software
462 (Vidrio Technologies). GCaMP6f and tdTomato were excited a using a pulsed dispersion-
463 compensated Ti:Sapphire laser (Coherent; Chameleon Vision II) tuned to 940 nm (40–80 mW at
464 the sample). Mice were head-fixed above a freely rotating circular treadmill consisting of a 6"
465 plastic saucer (Ware Manufacturing) mounted on a rotary encoder (US Digital, Serial #: MA3-A10-
466 125-B). Motorized, fixed-distance and velocity trials were conducted by connecting a integrated
467 servo motor (Teknic Clearpath: CPM-MCVC-2310S-RQN) to the treadmill to impose 10 s-long
468 running bouts every 20 s at 3 different speeds (6, 9 and 12 cm/s). Mouse posture was
469 simultaneously monitored using a near infrared camera (Basler; acA2000-165um), with each
470 video frame triggered by the two-photon imaging frame clock. The latter was recorded in
471 Wavesurfer (https://www.janelia.org/open-science/wavesurfer) to synchronize imaging and
472 behavioral data. Striatal fields of view (500 x 500 µm; 1–3 per mouse) near the center of the

473 imaging window were selected based on the expression of GCaMP6f and tdTomato, and were
474 continuously imaged with a resolution of 512 x 512 pixels at 30 Hz frame rate for a minimum of
475 20 min each. Bleaching of GCaMP6f was negligible over this time frame. The same fields of view
476 were imaged multiple times on non-consecutive days using alignment based on blood vessels
477 and a reference image.
478
479 **Image Processing.** Time series of two-photon images were concatenated and motion corrected,
480 and Ca^{2+} fluorescence traces were extracted from individual neurons with minimal neuropil
481 contamination using a custom MATLAB (Mathworks) pipeline described in detail in Driscoll et al.
482 (2017) and kindly made available by Chris Harvey (Harvard Medical School;
483 https://github.com/HarveyLab/Acquisition2P_class.git). Briefly, putative cell bodies were
484 selected manually in the mean intensity image. Highly correlated and spatially-contiguous
485 fluorescence sources within 30 µm of the selected pixel were then identified automatically based
486 on the correlation structure of the pixel time series to delineate the spatial footprint of active
487 neuronal processes. Fluorescence time series were computed by averaging across all pixels
488 within that footprint and were manually classified into cell bodies, processes (not analyzed), and
489 background (neuropil). This approach is advantageous over manually defined regions of interest
490 as it segregates dendritic processes that overlap with somata if they exhibit distinct fluorescence
491 time series. Each putative cell was paired with a neighboring background source, which was
492 subtracted from the cell body's fluorescence time series. Segmentation and neuropil subtraction
493 were manually verified for each cell and adjusted when necessary using a graphical user interface
494 to obtain clean neuropil-subtracted fluorescence traces without apparent negative-going
495 transients. GCamp6f-labelled cell bodies were manually labeled as a dSPNs based on tdTomato
496 fluorescence in the mean intensity image, and tdTomato-negative cells were labeled as putative
497 iSPNs or 'other' (not analyzed) based on cell morphology, baseline Ca^{2+} fluorescence intensity
498 and Ca^{2+} transient kinetics (**Fig. 1** and **Supplementary Fig. 1**) by an experimenter blind to
499 experimental conditions.
500
501 **Image and behavior analyses.** Quantification of imaging and behavioral data was carried out in
502 MATLAB using custom-code available online (https://github.com/TritschLab). Ca^{2+} transients
503 were detected using the built-in MATLAB findpeaks() function on each cell's neuropil-subtracted
504 fluorescence trace smoothed with a 150 ms window if they exhibited a minimum peak height
505 and minimum peak prominence of 5 standard deviations greater than baseline, and a minimum
506 width of 140 ms at half peak prominence. These criteria are intentionally stringent so as to
507 exclude events not clearly resolved from baseline fluorescence at the cost of underestimating
508 Ca^{2+} transient frequency per SPN. Ca^{2+} transient rise time is defined as the time required for
509 fluorescence to rise from 20 to 80 % of peak height, and decay time as the time required for
510 fluorescence to decay to one third of its peak. All imaged neurons displaying at minimum one

511 Ca^{2+} transient were deemed active. Individual fields of view were only selected for longitudinal
512 imaging and quantification if at least five active dSPNs and five active iSPNs were observed at
513 baseline in self-initiated and motorized locomotor trials, and if mice traveled at minimum five
514 meters in self-initiated trials to ensure adequate estimation of SPN ensemble size and mean SPN
515 Ca^{2+} transient frequency. For each imaging session and field of view, we report the fraction of all
516 dSPNs and iSPNs that display Ca^{2+} transients (i.e. active dSPN and iSPN ensemble size), the
517 frequency of Ca^{2+} transients recorded per active dSPNs or iSPNs while moving or immobile
518 averaged across each FOV, and the mean amplitude of Ca^{2+} transients recorded in all active dSPNs
519 or iSPNs averaged for each FOV. Population-level Ca^{2+} event rates in **Fig. 2** were calculated by
520 summing all Ca^{2+} transients imaged across the entire population of dSPNs and iSPNs in each FOV,
521 divided by the amount of time spent moving or remaining immobile. Activity in dSPNs and iSPNs
522 was compared for each imaging session and field of view by computing a bias index, consisting
523 of the difference in ensemble size, mean Ca^{2+} transient frequency or amplitude between dSPNs
524 and iSPNs, divided by their sum. Treadmill velocity was extracted from positional information
525 provided by the rotary encoder, down-sampled to 30 Hz and aligned to the two-photon imaging
526 frame rate. Immobility is defined as any period of time beginning at least 0.5 s after treadmill
527 velocity decreases below 0.2 cm/s, lasting at minimum 4 s, and ending 0.5 s before treadmill
528 velocity exceeds 0.2 cm/s again and for which no postural movement is detected using the
529 infrared camera. Movement bouts are defined as any period of time when absolute treadmill
530 velocity exceeds 0.4 cm/s for a minimum of 4 s, and is preceded and followed by 4 s of immobility.
531 Movement onsets and offsets are the first and last time points, respectively, at least two standard
532 deviations away from treadmill velocity measured while immobile. To relate Ca^{2+} transient
533 frequency to treadmill velocity, we determined treadmill speed for each recorded Ca^{2+} transient
534 and divided the total number of Ca^{2+} transients per velocity (binned to 0.4 cm/s) per SPN by the
535 amount of time spent by a mouse at that velocity over the course of an imaging session. To relate
536 the fraction of active SPNs to velocity, we averaged treadmill velocity in 200 ms bins, determined
537 the fraction of all imaged dSPNs or iSPNs active within each bin and calculated the mean
538 percentage of active dSPNs and iSPNs at different treadmill speeds (binned to 0.4 cm/s). To align
539 the fraction of active cells to movement onset/offset, we calculated the mean percentage of SPNs
540 exhibiting Ca^{2+} transients in 200 ms-long bins around all locomotor bout onsets/offsets. For
541 frequency of Ca^{2+} transients per movement onset/offset, we performed a similar procedure
542 except that the mean number of Ca^{2+} transients imaged per FOV per bin was further divided by
543 the total number of active SPNs and bin duration.
544
545 **Statistical analyses.** Data (reported in text and Figures as mean ± SEM) were compared in Prism
546 8 (Graphpad) using Mann-Whitney U test for independent groups, Wilcoxon signed-rank test for
547 matched samples and Two-way ANOVAs (Mixed-effect model) for all multiple comparison, as
548 indicated in text and figure legends. Significant interactions were followed-up with within-group

549 pairwise t-tests with baseline or prelesion data corrected for multiple comparisons (Bonferroni).
550 P values smaller than 0.05 were considered statistically significant and assigned the following
551 nomenclature in Figures: * $p < 0.05$, ** $p < 0.01$, *** $p < 0.005$ and **** $p < 0.001$. Reported n
552 values represent the number of fields of view imaged from N mice.

553 **REFERENCES**

554

555 Ade KK, Wan Y, Chen M, Gloss B, Calakos N. 2011. An Improved BAC Transgenic Fluorescent
556 Reporter Line for Sensitive and Specific Identification of Striatonigral Medium Spiny
557 Neurons. *Front Syst Neurosci* 5: 32
558 Barbera G, Liang B, Zhang L, Gerfen CR, Culurciello E, et al. 2016. Spatially Compact Neural
559 Clusters in the Dorsal Striatum Encode Locomotion Relevant Information. *Neuron* 92:
560 202-13
561 Bittner KC, Milstein AD, Grienberger C, Romani S, Magee JC. 2017. Behavioral time scale
562 synaptic plasticity underlies CA1 place fields. *Science* 357: 1033-36
563 Bloem B, Huda R, Sur M, Graybiel AM. 2017. Two-photon imaging in mice shows striosomes and
564 matrix have overlapping but differential reinforcement-related responses. *Elife* 6
565 Calabresi P, Picconi B, Tozzi A, Ghiglieri V, Di Filippo M. 2014. Direct and indirect pathways of
566 basal ganglia: a critical reappraisal. *Nat Neurosci* 17: 1022-30
567 Carter AG, Sabatini BL. 2004. State-dependent calcium signaling in dendritic spines of striatal
568 medium spiny neurons. *Neuron* 44: 483-93
569 Cenci MA. 2014. Presynaptic Mechanisms of l-DOPA-Induced Dyskinesia: The Findings, the
570 Debate, and the Therapeutic Implications. *Front Neurol* 5: 242
571 Chen TW, Wardill TJ, Sun Y, Pulver SR, Renninger SL, et al. 2013. Ultrasensitive fluorescent
572 proteins for imaging neuronal activity. *Nature* 499: 295-300
573 Churchland MM, Shenoy KV. 2007. Temporal complexity and heterogeneity of single-neuron
574 activity in premotor and motor cortex. *J Neurophysiol* 97: 4235-57
575 Cicchetti F, Brownell AL, Williams K, Chen YI, Livni E, Isacson O. 2002. Neuroinflammation of the
576 nigrostriatal pathway during progressive 6-OHDA dopamine degeneration in rats
577 monitored by immunohistochemistry and PET imaging. *Eur J Neurosci* 15: 991-8
578 Cui G, Jun SB, Jin X, Pham MD, Vogel SS, et al. 2013. Concurrent activation of striatal direct and
579 indirect pathways during action initiation. *Nature* 494: 238-42
580 da Silva JA, Tecuapetla F, Paixao V, Costa RM. 2018. Dopamine neuron activity before action
581 initiation gates and invigorates future movements. *Nature* 554: 244-48
582 Driscoll LN, Pettit NL, Minderer M, Chettih SN, Harvey CD. 2017. Dynamic Reorganization of
583 Neuronal Activity Patterns in Parietal Cortex. *Cell* 170: 986-99 e16
584 Dudman JT, Krakauer JW. 2016. The basal ganglia: from motor commands to the control of
585 vigor. *Curr Opin Neurobiol* 37: 158-66
586 Ellens DJ, Leventhal DK. 2013. Review: electrophysiology of basal ganglia and cortex in models
587 of Parkinson disease. *J Parkinsons Dis* 3: 241-54
588 Fieblinger T, Graves SM, Sebel LE, Alcacer C, Plotkin JL, et al. 2014. Cell type-specific plasticity of
589 striatal projection neurons in parkinsonism and L-DOPA-induced dyskinesia. *Nat*
590 *Commun* 5: 5316
591 Geddes CE, Li H, Jin X. 2018. Optogenetic Editing Reveals the Hierarchical Organization of
592 Learned Action Sequences. *Cell* 174: 32-43 e15
593 Gerfen CR, Surmeier DJ. 2011. Modulation of striatal projection systems by dopamine. *Annu*
594 *Rev Neurosci* 34: 441-66

595 Gittis AH, Kreitzer AC. 2012. Striatal microcircuitry and movement disorders. *Trends Neurosci*
596 35: 557-64
597 Graybiel AM. 2005. The basal ganglia: learning new tricks and loving it. *Curr Opin Neurobiol* 15:
598 638-44
599 Gritton HJ, Howe WM, Romano MF, DiFeliceantonio AG, Kramer MA, et al. 2019. Unique
600 contributions of parvalbumin and cholinergic interneurons in organizing striatal
601 networks during movement. *Nat Neurosci* 22: 586-97
602 Guo Q, Wang D, He X, Feng Q, Lin R, et al. 2015. Whole-brain mapping of inputs to projection
603 neurons and cholinergic interneurons in the dorsal striatum. *PLoS One* 10: e0123381
604 Helmchen F, Denk W. 2005. Deep tissue two-photon microscopy. *Nat Methods* 2: 932-40
605 Howe M, Ridouh I, Allegra Mascaro AL, Larios A, Azcorra M, Dombeck DA. 2019. Coordination of
606 rapid cholinergic and dopaminergic signaling in striatum during spontaneous movement.
607 *Elife* 8
608 Howe MW, Dombeck DA. 2016. Rapid signalling in distinct dopaminergic axons during
609 locomotion and reward. *Nature* 535: 505-10
610 Jedrzejewska-Szmek J, Damodaran S, Dorman DB, Blackwell KT. 2017. Calcium dynamics predict
611 direction of synaptic plasticity in striatal spiny projection neurons. *Eur J Neurosci* 45:
612 1044-56
613 Kerr JN, Plenz D. 2002. Dendritic calcium encodes striatal neuron output during up-states. *J*
614 *Neurosci* 22: 1499-512
615 Ketzef M, Spigolon G, Johansson Y, Bonito-Oliva A, Fisone G, Silberberg G. 2017. Dopamine
616 Depletion Impairs Bilateral Sensory Processing in the Striatum in a Pathway-Dependent
617 Manner. *Neuron* 94: 855-65 e5
618 Kincaid AE, Zheng T, Wilson CJ. 1998. Connectivity and convergence of single corticostriatal
619 axons. *J Neurosci* 18: 4722-31
620 Klaus A, Alves da Silva J, Costa RM. 2019. What, If, and When to Move: Basal Ganglia Circuits
621 and Self-Paced Action Initiation. *Annu Rev Neurosci* 42: 459-83
622 Klaus A, Martins GJ, Paixao VB, Zhou P, Paninski L, Costa RM. 2017. The Spatiotemporal
623 Organization of the Striatum Encodes Action Space. *Neuron* 96: 949
624 Kress GJ, Yamawaki N, Wokosin DL, Wickersham IR, Shepherd GM, Surmeier DJ. 2013.
625 Convergent cortical innervation of striatal projection neurons. *Nat Neurosci* 16: 665-7
626 Lemos JC, Friend DM, Kaplan AR, Shin JH, Rubinstein M, et al. 2016. Enhanced GABA
627 Transmission Drives Bradykinesia Following Loss of Dopamine D2 Receptor Signaling.
628 *Neuron* 90: 824-38
629 Lerner TN, Kreitzer AC. 2011. Neuromodulatory control of striatal plasticity and behavior. *Curr*
630 *Opin Neurobiol* 21: 322-7
631 Liang L, DeLong MR, Papa SM. 2008. Inversion of dopamine responses in striatal medium spiny
632 neurons and involuntary movements. *J Neurosci* 28: 7537-47
633 Mallet N, Ballion B, Le Moine C, Gonon F. 2006. Cortical inputs and GABA interneurons
634 imbalance projection neurons in the striatum of parkinsonian rats. *J Neurosci* 26: 3875-
635 84
636 Markowitz JE, Gillis WF, Beron CC, Neufeld SQ, Robertson K, et al. 2018. The Striatum Organizes
637 3D Behavior via Moment-to-Moment Action Selection. *Cell* 174: 44-58 e17

638 Meng C, Zhou J, Papaneri A, Peddada T, Xu K, Cui G. 2018. Spectrally Resolved Fiber Photometry
639 for Multi-component Analysis of Brain Circuits. *Neuron* 98: 707-17 e4
640 Nanou E, Catterall WA. 2018. Calcium Channels, Synaptic Plasticity, and Neuropsychiatric
641 Disease. *Neuron* 98: 466-81
642 Nelson AB, Kreitzer AC. 2014. Reassessing models of basal ganglia function and dysfunction.
643 *Annu Rev Neurosci* 37: 117-35
644 Nonomura S, Nishizawa K, Sakai Y, Kawaguchi Y, Kato S, et al. 2018. Monitoring and Updating of
645 Action Selection for Goal-Directed Behavior through the Striatal Direct and Indirect
646 Pathways. *Neuron* 99: 1302-14 e5
647 Owen SF, Berke JD, Kreitzer AC. 2018. Fast-Spiking Interneurons Supply Feedforward Control of
648 Bursting, Calcium, and Plasticity for Efficient Learning. *Cell* 172: 683-95 e15
649 Panigrahi B, Martin KA, Li Y, Graves AR, Vollmer A, et al. 2015. Dopamine Is Required for the
650 Neural Representation and Control of Movement Vigor. *Cell* 162: 1418-30
651 Parker JG, Marshall JD, Ahanonu B, Wu YW, Kim TH, et al. 2018. Diametric neural ensemble
652 dynamics in parkinsonian and dyskinetic states. *Nature* 557: 177-82
653 Parker PR, Lalive AL, Kreitzer AC. 2016. Pathway-Specific Remodeling of Thalamostriatal
654 Synapses in Parkinsonian Mice. *Neuron* this issue
655 Picconi B, Hernandez LF, Obeso JA, Calabresi P. 2018. Motor complications in Parkinson's
656 disease: Striatal molecular and electrophysiological mechanisms of dyskinesias. *Mov*
657 *Disord* 33: 867-76
658 Ponzi A, Wickens JR. 2013. Optimal balance of the striatal medium spiny neuron network. *PLoS*
659 *Comput Biol* 9: e1002954
660 Reig R, Silberberg G. 2014. Multisensory integration in the mouse striatum. *Neuron* 83: 1200-12
661 Robbe D. 2018. To move or to sense? Incorporating somatosensory representation into striatal
662 functions. *Curr Opin Neurobiol* 52: 123-30
663 Ryan MB, Bair-Marshall C, Nelson AB. 2018. Aberrant Striatal Activity in Parkinsonism and
664 Levodopa-Induced Dyskinesia. *Cell Rep* 23: 3438-46 e5
665 Sales-Carbonell C, Taouali W, Khalki L, Pasquet MO, Petit LF, et al. 2018. No Discrete Start/Stop
666 Signals in the Dorsal Striatum of Mice Performing a Learned Action. *Curr Biol* 28: 3044-
667 55 e5
668 Sauerbrei B, Guo JZ, Mischiati M, Guo W, Kabra M, et al. 2018. Motor cortex is an input-driven
669 dynamical system controlling dexterous movement. In *BioRxiv*. BioRxiv
670 Shen W, Flajolet M, Greengard P, Surmeier DJ. 2008. Dichotomous dopaminergic control of
671 striatal synaptic plasticity. *Science* 321: 848-51
672 Sheng MJ, Lu D, Shen ZM, Poo MM. 2019. Emergence of stable striatal D1R and D2R neuronal
673 ensembles with distinct firing sequence during motor learning. *Proc Natl Acad Sci U S A*
674 116: 11038-47
675 Stephenson-Jones M, Yu K, Ahrens S, Tucciarone JM, van Huijstee AN, et al. 2016. A basal
676 ganglia circuit for evaluating action outcomes. *Nature* 539: 289-93
677 Tai LH, Lee AM, Benavidez N, Bonci A, Wilbrecht L. 2012. Transient stimulation of distinct
678 subpopulations of striatal neurons mimics changes in action value. *Nat Neurosci* 15:
679 1281-9
680 Tepper JM, Wilson CJ, Koos T. 2008. Feedforward and feedback inhibition in neostriatal
681 GABAergic spiny neurons. *Brain Res Rev* 58: 272-81

682 Thiele SL, Warre R, Nash JE. 2012. Development of a unilaterally-lesioned 6-OHDA mouse model
683 of Parkinson's disease. *J Vis Exp*
684 Tritsch NX, Sabatini BL. 2012. Dopaminergic modulation of synaptic transmission in cortex and
685 striatum. *Neuron* 76: 33-50
686 Trudeau LE, Hnasko TS, Wallen-Mackenzie A, Morales M, Rayport S, Sulzer D. 2014. The
687 multilingual nature of dopamine neurons. *Prog Brain Res* 211: 141-64
688 Turner RS, Desmurget M. 2010. Basal ganglia contributions to motor control: a vigorous tutor.
689 *Curr Opin Neurobiol* 20: 704-16
690 Vijayraghavan S, Wang M, Birnbaum SG, Williams GV, Arnsten AF. 2007. Inverted-U dopamine
691 D1 receptor actions on prefrontal neurons engaged in working memory. *Nat Neurosci*
692 10: 376-84
693 Wall NR, De La Parra M, Callaway EM, Kreitzer AC. 2013. Differential innervation of direct- and
694 indirect-pathway striatal projection neurons. *Neuron* 79: 347-60
695 Willard AM, Isett BR, Whalen TC, Mastro KJ, Ki CS, et al. 2019. State transitions in the substantia
696 nigra reticulata predict the onset of motor deficits in models of progressive dopamine
697 depletion in mice. *Elife* 8
698 Wilson CJ, Kawaguchi Y. 1996. The origins of two-state spontaneous membrane potential
699 fluctuations of neostriatal spiny neurons. *J Neurosci* 16: 2397-410
700 Yin HH, Mulcare SP, Hilario MR, Clouse E, Holloway T, et al. 2009. Dynamic reorganization of
701 striatal circuits during the acquisition and consolidation of a skill. *Nat Neurosci* 12: 333-
702 41
703 Yttri EA, Dudman JT. 2018. A Proposed Circuit Computation in Basal Ganglia: History-Dependent
704 Gain. *Mov Disord* 33: 704-16
705 Zhai S, Shen W, Graves SM, Surmeier DJ. 2019. Dopaminergic modulation of striatal function
706 and Parkinson's disease. *J Neural Transm (Vienna)* 126: 411-22
707 Zhou P, Resendez SL, Rodriguez-Romaguera J, Jimenez JC, Neufeld SQ, et al. 2018. Efficient and
708 accurate extraction of in vivo calcium signals from microendoscopic video data. *Elife* 7
709 Zhuang X, Mazzoni P, Kang UJ. 2013. The role of neuroplasticity in dopaminergic therapy for
710 Parkinson disease. *Nat Rev Neurol* 9: 248-56
711 Ziv Y, Ghosh KK. 2015. Miniature microscopes for large-scale imaging of neuronal activity in
712 freely behaving rodents. *Curr Opin Neurobiol* 32: 141-7
713
714

Figure 1

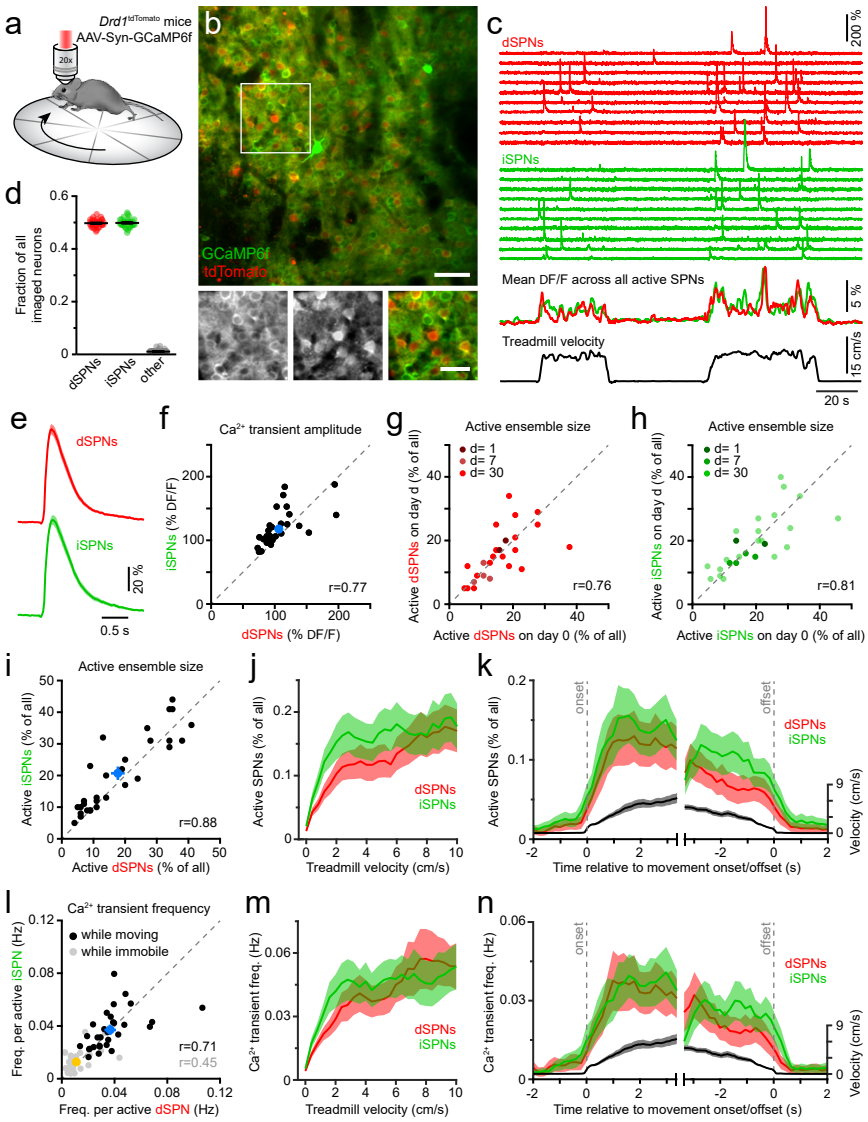
a
Drd1tdTomato mice
AAV-Syn-GCaMP6f
20x
b
GCaMP6f
tdTomato
c
dSPNs
iSPNs
200 %
Mean DF/F across all active SPNs
5 %
Treadmill velocity
15 cm/s
20 s
d
Fraction of all imaged neurons
dSPNs
iSPNs
other
e
dSPNs
iSPNs
20 %
0.5 s
f
Ca2+ transient amplitude
iSPNs (% DF/F)
dSPNs (% DF/F)
r=0.77
g
Active ensemble size
d= 1
d= 7
d= 30
Active dSPNs on day d (% of all)
Active dSPNs on day 0 (% of all)
r=0.76
h
Active ensemble size
Active iSPNs on day d (% of all)
Active iSPNs on day 0 (% of all)
r=0.81
i
Active ensemble size
Active iSPNs (% of all)
Active dSPNs (% of all)
r=0.88
j
Active SPNs (% of all)
dSPNs
iSPNs
Treadmill velocity (cm/s)
k
Active SPNs (% of all)
onset
offset
dSPNs
iSPNs
Velocity (cm/s)
Time relative to movement onset/offset (s)
l
Ca2+ transient frequency
while moving
while immobile
Freq. per active iSPN (Hz)
Freq. per active dSPN (Hz)
r=0.71
r=0.45
m
Ca2+ transient freq. (Hz)
dSPNs
iSPNs
Treadmill velocity (cm/s)
n
Ca2+ transient freq. (Hz)
onset
offset
dSPNs
iSPNs
Velocity (cm/s)
Time relative to movement onset/offset (s)

Figure 1. Simultaneous Ca^{2+} imaging from dSPNs and iSPNs

a. Schematic of experimental setup.

b. *Top*: representative two-photon maximum projection image of dorsolateral striatum. Red: td-tomato labelled dSPNs, green: striatal neurons virally transduced to express GCaMP6f (scale bar: 50 μm). *Inset* shown at *bottom* in green (*left*) and red (*middle*) channels only, and composite (*right*; scale: 30 μm).

c. *Top*: example Ca^{2+} fluorescence traces from dSPNs (red) and putative iSPNs (green). *Middle*: Mean $\Delta F/F$ across all active dSPNs and iSPNs. *Bottom*: treadmill velocity highlighting two self-initiated locomotor bouts.

d. Proportion of all imaged neurons assigned to dSPNs, iSPNs and other neurons (n = 30 FOVs in 18 mice).

e. Mean Ca^{2+} transient waveform (± SEM) imaged from active dSPNs and iSPNs.

f. Comparison of Ca^{2+} transient amplitude in dSPNs versus iSPNs. Correlation coefficient r is indicated in plot and mean ± SEM in blue (p = 0.004; Wilcoxon signed-ranks; n = 30 FOVs).

g. Comparable percentages of dSPNs exhibit Ca^{2+} transients in the same FOV on imaging sessions separated by d days (p = 0.76; Wilcoxon signed-ranks; n = 30 FOVs).

h. Same as **g** for iSPNs (p = 0.78; Wilcoxon signed-ranks).

i. Percentage of imaged dSPNs and iSPNs exhibiting Ca^{2+} transients per FOV (n = 30). Mean ± SEM shown in blue.

j. Percentage of all imaged dSPNs and iSPNs that display Ca^{2+} transients at different treadmill velocities (n = 30 FOVs).

k. Percentage of all imaged dSPNs and iSPNs that display Ca^{2+} transients aligned to locomotion onset (left) and offset (right) overlaid with treadmill velocity (black).

l. Mean Ca^{2+} transient frequency in all active dSPNs vs. iSPNs (n = 30 FOVs) during spontaneous treadmill running (black) and while immobile (gray). No significant difference was observed between dSPNs and iSPNs while moving (blue; p = 0.8, Wilcoxon signed-ranks) or immobile (yellow; p = 0.4, Wilcoxon signed-ranks).

m. Same as **j** for Ca^{2+} transient frequency in dSPNs and iSPNs.

n. Same as **k** for Ca^{2+} transient frequency in dSPNs and iSPNs.

Data in **j**, **k**, **m** and **n** represent mean ± SEM. dSPNs are shown in red, iSPNs in green.

Figure 2

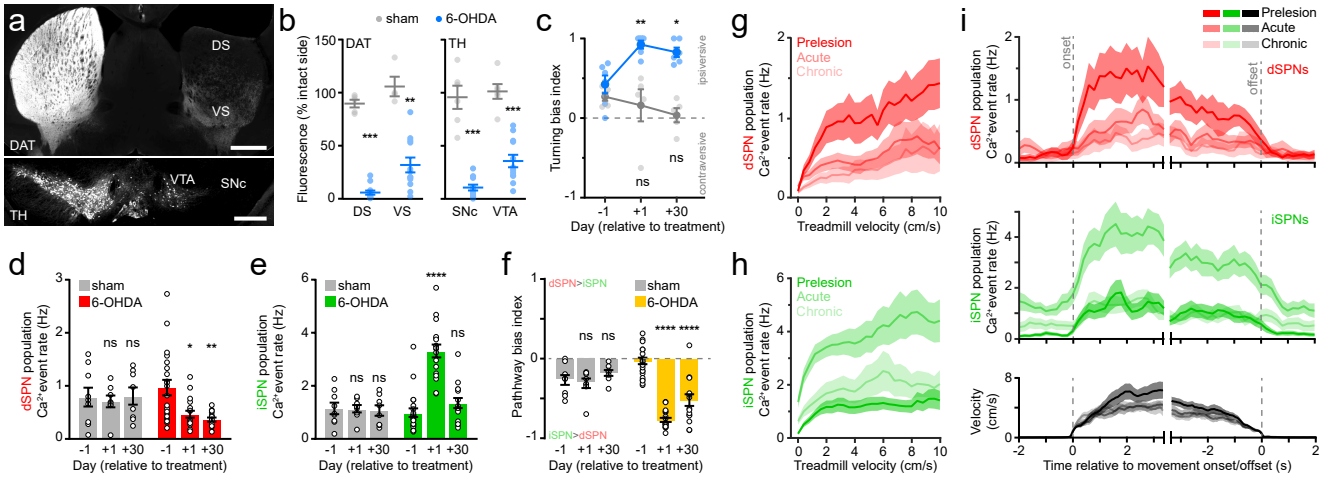
a
DS
VS
DAT
VTA
SNc
TH
b
sham
6-OHDA
DAT
TH
Fluorescence (% intact side)
DS
VS
SNc
VTA
c
Turning bias index
ipsiversive
contraversive
Day (relative to treatment)
g
Prelesion
Acute
Chronic
dSPN population Ca2+event rate (Hz)
Treadmill velocity (cm/s)
i
Prelesion
Acute
Chronic
onset
offset
dSPNs
iSPNs
iSPN population Ca2+event rate (Hz)
Velocity (cm/s)
Time relative to movement onset/offset (s)
d
sham
6-OHDA
dSPN population Ca2+event rate (Hz)
Day (relative to treatment)
e
sham
6-OHDA
iSPN population Ca2+event rate (Hz)
Day (relative to treatment)
f
dSPN>iSPN
iSPN>dSPN
sham
6-OHDA
Pathway bias index
Day (relative to treatment)
h
Prelesion
Acute
Chronic
iSPN population Ca2+event rate (Hz)
Treadmill velocity (cm/s)

Figure 2. SNc neuron loss differentially affects population-level Ca^{2+} event rate in dSPNs and iSPNs

a. Representative coronal forebrain (*top*) and ventral midbrain (*bottom*) sections from a mouse injected with 6-OHDA into the right SNc and stained for DAT (*top*) and TH (*bottom*). DS, dorsal striatum; VS, ventral striatum; VTA, ventral tegmental area. Scale bars: 1 mm (*top*), 0.5 mm (*bottom*).

b. Quantification of immunofluorescence signal for DAT in dorsal and ventral striatum (*left*) and TH in SNc and VTA (*right*) in sham (gray; N = 6) and 6-OHDA lesioned (blue; N = 12) mice on treated vs. intact hemispheres (mean ± SEM overlaid). Asterisks depict significant difference from sham (DS: $p = 3.2 \times 10^{-4}$; VS: $p = 0.001$; SNc: $p = 1.1 \times 10^{-4}$; VTA: $p = 1.1 \times 10^{-4}$; Mann-Whitney).

c. Turning bias measured in a closed-arm plus maze from a subset of vehicle (N = 5, gray) and 6-OHDA injected (N = 6, blue) mice 1 day before, 1 day after and 30 days after intracranial injection surgery. Values approaching 1 and -1 reflect strong turning bias toward (ipsiversive) or away from (contraversive) the lesioned hemisphere, respectively. Within-group post-hoc statistic (Bonferroni, vs. pre-surgery): Sham, day 1: $p = 0.98$; day 30: $p = 0.28$; 6-OHDA, day 1: $p = 0.003$; day 30: $p = 0.015$.

d. Mean (± SEM) Ca^{2+} event rate across the entire population of dSPNs per FOV during self-initiated movement before, 1 day after or 30 days after ipsilateral sham (n = 9 FOVs in 6 mice) or 6-OHDA lesion (n = 21 from 12 mice) of SNc neurons. Within-group post-hoc statistics (Bonferroni, vs. pre-surgery): Sham, day 1: $p > 0.99$; day 30: $p > 0.99$. 6-OHDA, day 1: $p = 0.011$; day 30: $p = 0.008$.

e. Same as **d** for iSPNs. Within-group post-hoc statistics (Bonferroni, vs. pre-surgery): Sham, day 1: $p > 0.99$; day 30: $p > 0.99$. 6-OHDA, day 1: $p = 1.9 \times 10^{-7}$; day 30: $p = 0.46$.

f. Same as **d** for Ca^{2+} event rate bias between pathways. Values approaching 1 and -1 reflect bias towards dSPNs and iSPNs, respectively. Within-group post-hoc statistics (Bonferroni, vs. pre-surgery): Sham, day 1: $p = 0.67$; day 30: $p = 0.59$. 6-OHDA, day 1: $p = 8.1 \times 10^{-12}$; day 30: $p = 8.4 \times 10^{-5}$.

g. Mean population-level Ca^{2+} event rate in dSPNs vs. treadmill velocity before, 1 day after or 30 days after SNc lesion (n = 21 FOVs). Shaded regions indicate SEM.

h. Same as **g** for iSPNs.

i. Same as **g** for dSPNs (*top*) and iSPNs (*middle*) vs. treadmill velocity (*bottom*) aligned to the onset (*left*) and offset (*right*) of locomotor bouts.

Figure 3

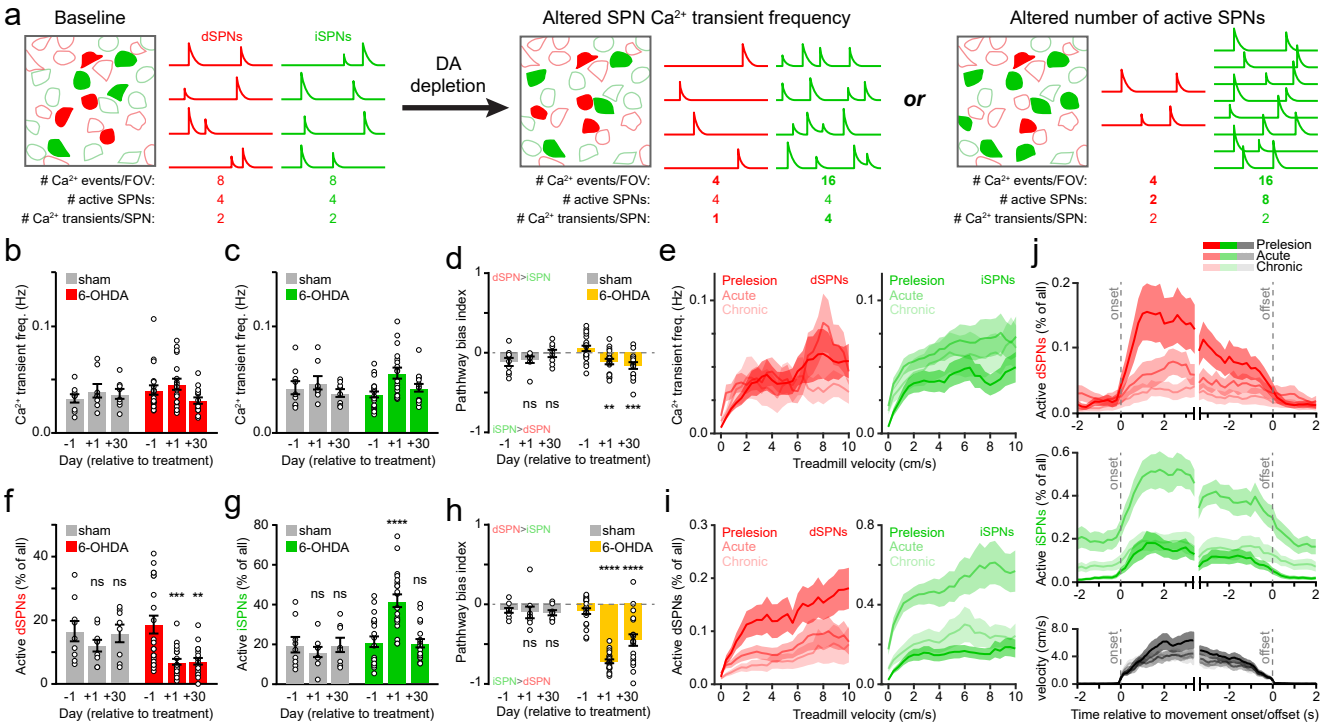
a
Baseline
dSPNs
iSPNs
Ca2+ events/FOV: 8 8
active SPNs: 4 4
Ca2+ transients/SPN: 2 2
DA depletion
Altered SPN Ca2+ transient frequency
Ca2+ events/FOV: 4 16
active SPNs: 4 4
Ca2+ transients/SPN: 1 4
or
Altered number of active SPNs
Ca2+ events/FOV: 4 16
active SPNs: 2 8
Ca2+ transients/SPN: 2 2
b
sham
6-OHDA
Ca2+ transient freq. (Hz)
Day (relative to treatment)
c
d
dSPN>iSPN
iSPN>dSPN
Pathway bias index
e
Prelesion
Acute
Chronic
dSPNs
iSPNs
Treadmill velocity (cm/s)
j
Active dSPNs (% of all)
Active iSPNs (% of all)
velocity (cm/s)
onset
offset
Time relative to movement onset/offset (s)
f
g
h
i

Figure 3. Lesioning DA neurons alters the number of active SPNs

a. Schematic of possible circuit mechanisms accounting for population-level Ca^{2+} event rate changes following DA depletion. *Left*: locomotion is associated with the activation of sparse subsets of SPNs that, over time, define action-specific dSPN and iSPN ensembles (filled neuronal profiles and their Ca^{2+} fluorescence signals. After DA depletion, population-level changes in Ca^{2+} event rate in all dSPNs and iSPNs per FOV may arise from modifying the frequency of Ca^{2+} transients in active SPNs (*middle*) or from altering the overall size of SPN ensembles associated with locomotion (*right*).

b. Mean (± SEM) Ca^{2+} transient frequency per dSPN active during self-initiated movement before, 1 day after, or 30 days after sham (n = 9 FOVs in 6 mice) or 6-OHDA-mediated (n = 21 FOVs from 12 mice) SNc ablation.

c. Same as **b** for iSPNs.

d. Same as **b** for Ca^{2+} transient frequency bias between pathways. Within-group post-hoc statistics (Bonferroni, vs. pre-surgery): Sham, day 1: $p > 0.99$; day 30: $p = 0.23$. 6-OHDA, day 1: $p = 0.008$; day 30: 5.0×10^{-4}.

e. Mean Ca^{2+} transient frequency per dSPN (*left*) and iSPN (*right*) vs. treadmill velocity before, 1 day after or 30 days after SNc lesion (n = 21 FOVs). Shaded regions indicate SEM.

f. Percentage of all imaged dSPNs that exhibit Ca^{2+} transients per FOV before, 1 day after, or 30 days after sham (n = 9 FOVs in 6 mice) or 6-OHDA-mediated (n = 21 FOVs from 12 mice) SNc lesion. Within-group post-hoc statistics (Bonferroni, vs. pre-surgery): Sham, day 1: $p = 0.42$; day 30: $p > 0.99$. 6-OHDA, day 1: $p = 1.8 \times 10^{-4}$; day 30: $p = 0.001$.

g. Same as **f** for iSPNs. Within-group post-hoc statistics (Bonferroni, vs. pre-surgery): Sham, day 1: $p = 0.78$; day 30: $p > 0.99$. 6-OHDA, day 1: $p = 8.0 \times 10^{-7}$; day 30: $p > 0.99$.

h. Same as **f** for bias in number of active cells per FOV between pathways. Within-group post-hoc statistics (Bonferroni, vs. pre-surgery): Sham, day 1: $p > 0.99$; day 30: $p > 0.99$. 6-OHDA, day 1: $p = 3.1 \times 10^{-14}$; day 30: $p = 4.2 \times 10^{-5}$.

i. Same as **e** for percentage of all imaged dSPNs (*left*) and iSPNs (*right*) that show Ca^{2+} transients at different treadmill velocities. Note similarities with **Fig. 2g, h**.

j. Percentage of dSPN and iSPN activated per self-initiated locomotor bout aligned to onset and offset before, 1 day after, or 30 days after 6-OHDA lesion. Note similarities with **Fig. 2i**.

Figure 4

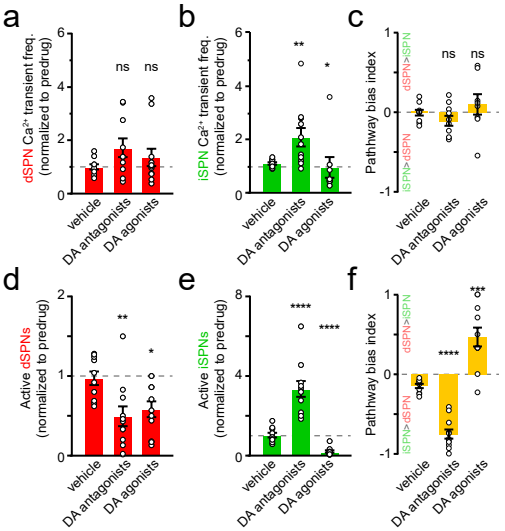
a
dSPN Ca2+ transient freq. (normalized to predrug)
ns
ns
vehicle
DA antagonists
DA agonists
b
iSPN Ca2+ transient freq. (normalized to predrug)
**
*
c
Pathway bias index
dSPN>iSPN
iSPN>dSPN
ns
ns
d
Active dSPNs (normalized to predrug)
**
*
e
Active iSPNs (normalized to predrug)
****
****
f
Pathway bias index
****
***

Figure 4. DA dynamically alters SPN ensemble size

a. Mean Ca^{2+} transient frequency per dSPN active during locomotion after systemic administration of vehicle (*left*; n = 10 FOVs in 5 mice), a cocktail of D1 and D2 receptor antagonists (*middle*; n = 11 FOVs in 5 mice, p = 0.20, Mann-Whitney) and a cocktail of D1 and D2 receptor agonists (*right*; n = 11 FOVs in 7 mice, p = 0.88, Mann-Whitney) normalized to pre-drug baseline.

b. Same as **a** for iSPNs (antagonists: p = 0.007; agonists: p = 0.02; Mann-Whitney).

c. Same as **a** for bias in frequency between pathways (antagonists: p = 0.22; agonists: p = 0.36; Mann-Whitney).

d. Fraction of all imaged dSPNs active per FOV after systemic administration of vehicle (*left*; n = 10 FOVs in 5 mice), D1 and D2 receptor antagonists (*middle*; n = 11 FOVs in 5 mice, p = 0.006, Mann-Whitney) or D1 and D2 receptor agonists (*right*; n = 11 FOVs in 7 mice, p = 0.015, Mann-Whitney) normalized to pre-drug baseline.

e. Same as **d** for iSPNs (antagonists: $p = 5.7 \times 10^{-6}$; agonists: $p = 2.3 \times 10^{-5}$; Mann-Whitney).

f. Same as **d** for bias in ensemble size between pathways (antagonists: $p = 5.7 \times 10^{-6}$; agonists: $p = 2.0 \times 10^{-4}$; Mann-Whitney).

Mean ± SEM are overlaid for each group. Asterisks depict significant difference from vehicle.

Figure 5

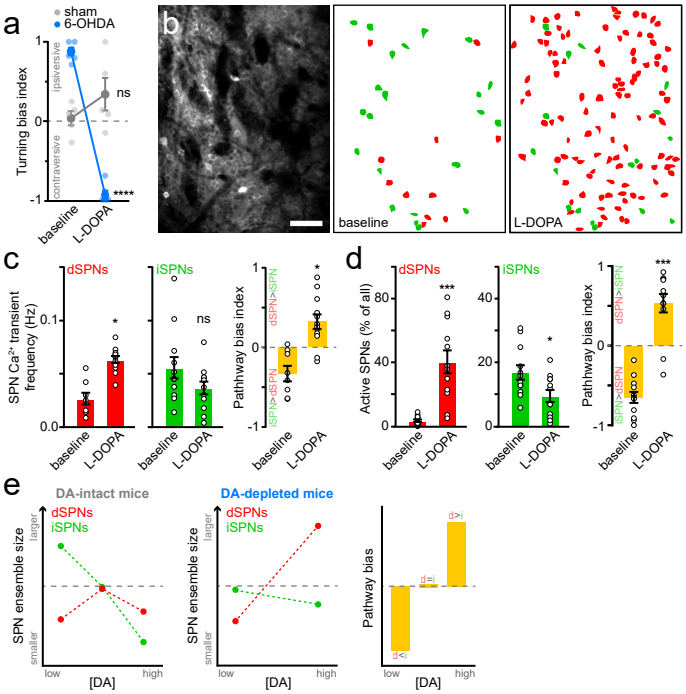
a
sham
6-OHDA
Turning bias index
ipsiversive
contraversive
ns
****
baseline
L-DOPA
b
baseline
L-DOPA
c
dSPNs
iSPNs
SPN Ca2+ transient frequency (Hz)
Pathway bias index
dSPN>iSPN
iSPN>dSPN
d
Active SPNs (% of all)
e
DA-intact mice
DA-depleted mice
SPN ensemble size
larger
smaller
low
high
[DA]
Pathway bias

Figure 5. SPN ensembles respond differently to DA in chronically DA-depleted striatum

a. Turning bias measured in closed-arm plus maze before and after L-DOPA treatment in a subset of DA-intact (N = 5, gray; p = 0.15 vs. baseline, post-hoc Bonferroni) and chronically DA-depleted mice (N = 6, blue; $p = 6.24 \times 10^{-10}$ vs. baseline, post-hoc Bonferroni).

b. Example maximum projection image of dorsal striatum (*left*) and spatial distribution of dSPNs (red) and iSPNs (green) displaying Ca^{2+} transients during imaging sessions immediately preceding (*middle*) and following (*right*) systemic L-DOPA administration. Scale bar: 50 μm.

c. Mean Ca^{2+} transient frequency per dSPN (*left*) and iSPN (*middle*) active in chronically-lesioned mice before and after elevating striatal DA with L-DOPA (n= 12 FOVs in 6 mice). *Right*: frequency bias index. Mean ± SEM are overlaid for each group (dSPN: p = 0.023; iSPN: p = 0.052; pathway bias: p = 0.016; all vs. baseline, Wilcoxon signed rank).

d. Same as **c** for active SPN ensemble size (dSPN: p = 0.001; iSPN: p = 0.016; pathway bias: $p = 4.9 \times 10^{-4}$; all vs. baseline, Wilcoxon signed rank).

e. Summary diagrams depicting observed changes in SPN ensemble size in response to changing striatal DA levels in intact and DA-depleted mice.

Supplementary Figure 1

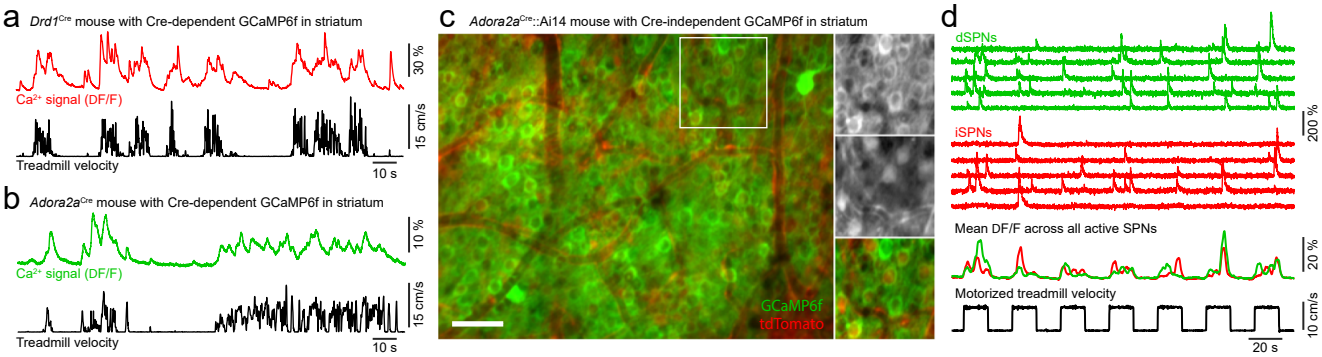

Supplementary Figure 1. dSPNs and iSPNs exhibit similar Ca^{2+} signals

a. Fiber-photometry recording (*top*) and treadmill velocity (*bottom*) recorded from a *Drd1*^{Cre} mouse virally expressing Cre-dependent GCaMP6f in dorsolateral striatum. Population Ca^{2+} fluorescence is most prominent during bouts of forward locomotion.

b. Same as **a** for an *Adora2a*^{Cre} mouse expressing GCaMP6f in iSPNs.

c. Representative *in vivo* two-photon maximum projection image of dorsolateral striatum in an *Adora2a*^{Cre} mouse expressing a red (tdTomato) Cre reporter in iSPNs (Ai14 line) and Cre-independent GCaMP6f virally (AAV-Syn-GCaMP6f) in all neurons. *Inset*: Detail of boxed area in green (*top*), red (*middle*) and merged (*bottom*) channels. Scale bar: 50 µm.

d. Example Ca^{2+} fluorescence traces from five active iSPNs (red) and five putative dSPNs (green) in FOV shown in **c**. Mean fluorescence signal in both pathways is highest during locomotor bouts on motorized treadmill (black).

Supplementary Figure 2

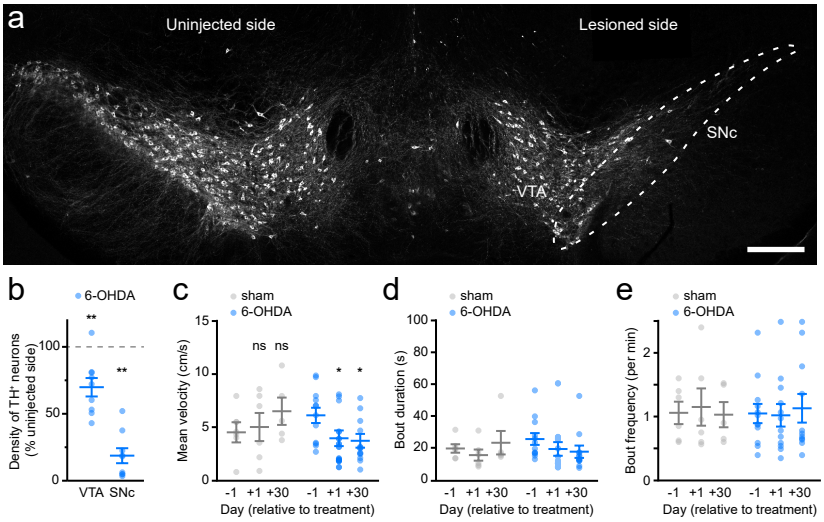

Supplementary Figure 2. Unilateral loss of SNc neurons mildly affects self-initiated treadmill locomotion

a. Representative confocal image of a coronal midbrain section stained for TH 24 h after unilateral lesion of SNc (dashed outline) with 6-OHDA. Scale bar: 300 μm.

b. Number of TH-positive neurons identified in SNc and VTA on injection side relative to contralateral side 24 h after intracranial injection (VTA, $p = 0.008$; SNc, $p = 0.004$, $n = 9$ sections from 3 mice, Wilcoxon signed rank).

c. Quantification of mean self-initiated treadmill velocity before, 1 day after and 30 days after unilateral injection of vehicle (N = 6, gray) or 6-OHDA (N = 12, blue) in SNc. Within-group post-hoc statistics (Bonferroni, vs. pre-surgery) for velocity: sham, day 1: $p > 0.99$; day 30: $p = 0.14$. 6-OHDA, day 1: $p = 0.035$; day 30: $p = 0.033$.

d. Same as **c** for locomotor bout duration.

e. Same as **c** for bout frequency.

Supplementary Figure 3

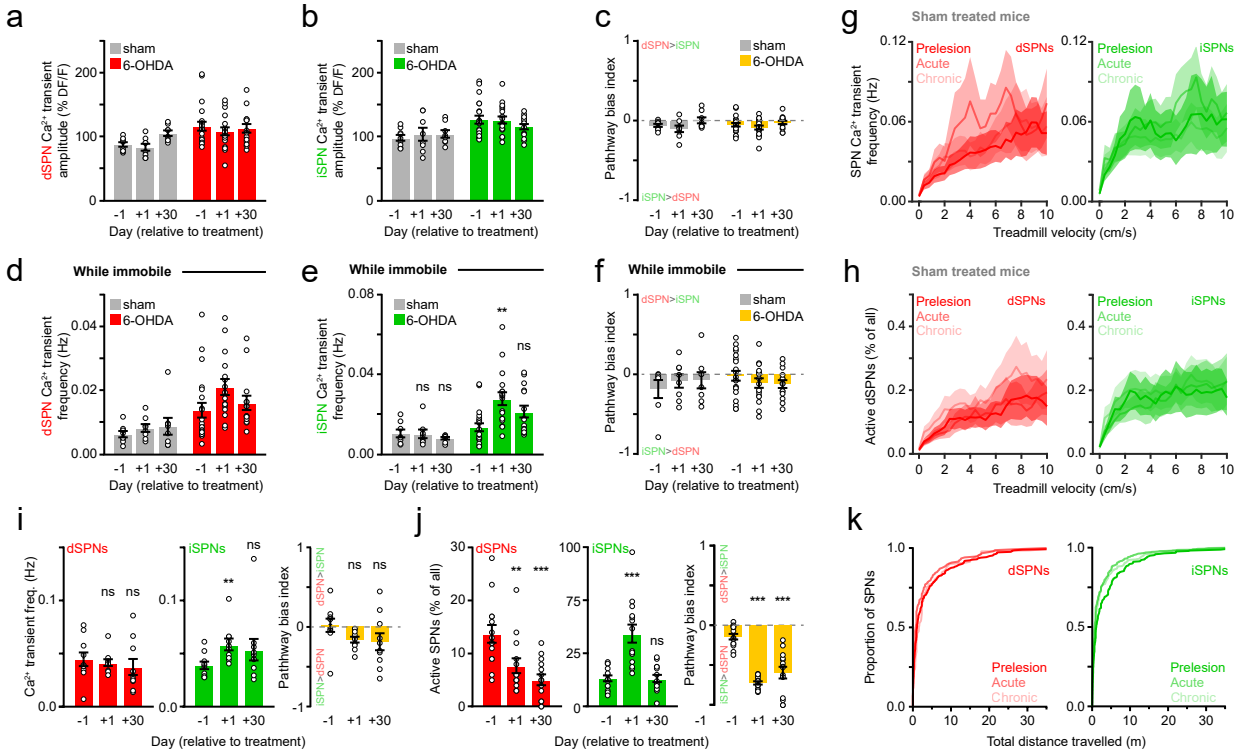

Supplementary Figure 3. Characterization of striatal activity in sham and 6-OHDA treated mice

a. Mean Ca^{2+} transient amplitude in dSPNs active during self-initiated movement immediately before, 1 day after and 30 days after vehicle (gray, n = 9 FOVs in 6 mice) or 6-OHDA (n = 21 FOVs in 12 mice) infusion in SNc.

b. Same as **a** for iSPNs.

c. Same as **a** for bias in amplitude between pathways.

d. Mean Ca^{2+} transient frequency per dSPN active while immobile immediately before, 1 day after and 30 days after vehicle (gray, n = 9 FOVs in 6 mice) or 6-OHDA (n = 21 FOVs in 12 mice) infusion in SNc. No significant interaction was detected between sham and 6-OHDA lesioned mice over time (Two-way ANOVA lesion x time: $F_{2,71} = 0.63$, $p = 0.54$).

e. Same as **d** for iSPNs. A significant interaction was detected between sham and 6-OHDA lesioned mice over time (Two-way ANOVA lesion x time: $F_{2,71} = 3.19$, $p = 0.0473$). Within-group post-hoc analyses (Bonferroni) revealed no significant changes in Ca^{2+} transient frequency in iSPNs sham mice ($p > 0.99$ vs. prelesion on day 1 and $p = 0.47$ vs. prelesion on day 30), but a significant increase in 6-OHDA injected mice on day 1 ($p = 0.006$ vs. pre-lesion) but not on day 30 ($p = 0.066$ vs. pre-lesion).

f. Same as **d** for Ca^{2+} transient frequency bias between pathways. No significant interaction was detected between sham and 6-OHDA lesioned mice over time (Two-way ANOVA lesion x time: $F_{2,67} = 1.12$, $p = 0.33$).

g. Mean ± SEM Ca^{2+} transient frequency per dSPN (*left*) and iSPN (*right*) versus treadmill velocity before, 1 day after (acute) or 30 days after (chronic) unilateral vehicle injection in SNc (n = 9 FOVs in 6 mice).

h. Same as **g** for the percentage of all imaged dSPNs or iSPNs that show Ca^{2+} transients at different treadmill velocities.

i. Mean Ca^{2+} transient frequency recorded in dSPNs (*left*) and iSPNs (*middle*) active during fixed-velocity locomotion on a motorized treadmill and their relative bias (*right*) immediately before, 1 day after or 30 days after unilateral 6-OHDA injection in SNc (dSPNs: day 1 $p = 0.70$ and day 30 $p = 0.56$; iSPNs: day 1 $p = 0.002$ and day 30 $p = 0.19$; pathway bias: day 1 $p = 0.065$ and day 30 $p = 0.084$; all vs. prelesion, Wilcoxon signed rank, n = 14 FOVs in 7 mice).

j. Same as **i** for the percentage of all imaged dSPNs or iSPNs exhibiting Ca^{2+} transients over the course of imaging sessions (dSPNs: day 1 $p = 0.003$ and day 30 $p = 3.7 \times 10^{-4}$; iSPNs: day 1 $p = 1.2 \times 10^{-4}$ and day 30 $p = 0.88$; pathway bias: day 1 $p = 1.2 \times 10^{-4}$ and day 30 $p = 1.2 \times 10^{-4}$; all vs. prelesion, Wilcoxon signed rank).

k. Cumulative distribution of the proportion of active dSPNs (*left*) and iSPNs (*right*) recruited vs. total distance travelled before (prelesion), 1 day after (acute) or 30 days after (chronic) unilateral 6-OHDA injection in SNc. More than 75% of ensemble size is captured within the first five meters travelled under all experimental conditions.

Supplementary Figure 4

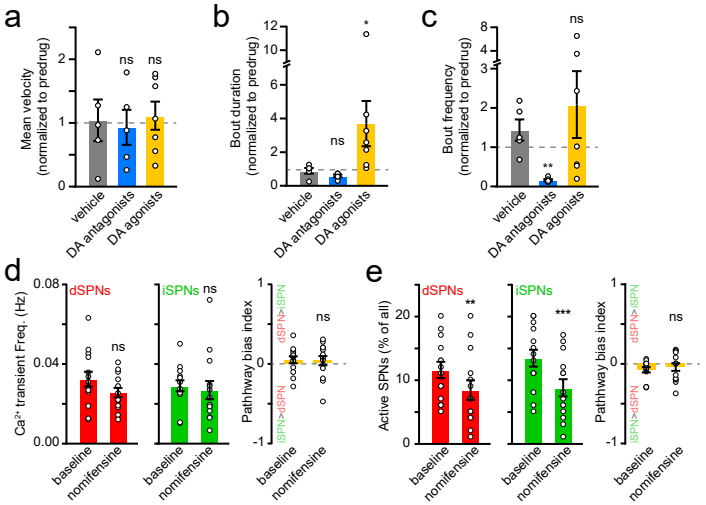

Supplementary Figure 4. Manipulating DA signaling pharmacologically alters locomotor behavior and SPN ensemble size

a. Mean self-initiated treadmill velocity after systemic administration of vehicle (N = 5 mice), D1 and D2 receptor antagonists (N = 5 mice, p = 0.84 vs. vehicle, Mann-Whitney) or D1 and D2 receptor agonists (N = 7 mice, p = 0.88 vs. vehicle, Mann-Whitney) normalized to pre-drug baseline.

b. Same as **a** for locomotor bout duration (D1 and D2 receptor antagonists: p = 0.15; D1 and D2 receptor agonists: p = 0.01; all vs. vehicle, Mann-Whitney).

c. Same as **a** for bout frequency (D1 and D2 receptor antagonists: p = 0.008; D1 and D2 receptor agonists: p = 0.88; all vs. vehicle, Mann-Whitney).

d. Mean Ca^{2+} transient frequency per dSPN (*left*) and iSPN (*middle*) active during locomotion on a motorized treadmill before and after pharmacological DA elevation with nomifensine. *Right*: frequency bias between pathways (dSPN: p = 0.24; iSPN: p = 0.58; pathway bias: p = 0.88; all vs. prelesion, Wilcoxon signed rank, n = 14 FOVs in 6 mice).

e. Same as **a** for active dSPNs and iSPNs ensemble size (dSPN: p = 0.005; iSPN: $p = 2.4 \times 10^{-4}$; pathway bias index: p = 0.68; all vs. prelesion, Wilcoxon signed rank).

Supplementary Video

Two-photon time lapse series (30 Hz frame rate) of Gcamp6f fluorescence in dorsolateral striatum as mice engage in bouts of self-paced forward locomotion. Replay speed: 1x.